NANO LETTERS

pubs.acs.org/NanoLett Letter

Ultrasensitive Photothermal Spectroscopy: Harnessing the Seebeck Effect for Attogram-Level Detection

Yaoli Zhao, Patatri Chakraborty, Ali Passian, and Thomas Thundat*

Cite This: https://doi.org/10.1021/acs.nanolett.3c01710 Read Online

ACCESS | Metrics & More | Article Recommendations | Supporting Information

ABSTRACT: Molecular-level spectroscopy is crucial for sensing and imaging applications, yet detecting and quantifying minuscule quantities of chemicals remain a challenge, especially when they surface adsorb in low numbers. Here, we introduce a photothermal spectroscopic technique that enables the high selectivity sensing of adsorbates with an attogram detection limit. Our approach utilizes the Seebeck effect in a microfabricated nanoscale thermocouple junction, incorporated into the apex of a microcantilever. We observe minimal thermal mass exhibited by the sensor, which maintains exceptional thermal insulation. The temperature variation driving the thermoelectric junction arises from the nonradiative decay of molecular adsorbates' vibrational states on the tip. We demonstrate the detection of photothermal spectra of physisorbed trinitrotoluene (TNT) and dimethyl methylphosphonate (DMMP) molecules, as well as representative polymers, with an estimated mass of 10^{-18} g.

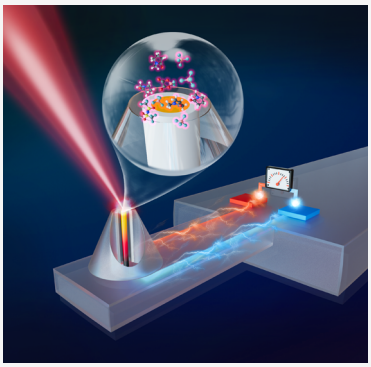

KEYWORDS: *molecular recognition, calorimetry, microfabricated thermocouple, photothermal spectroscopy, infrared sensor*

One of the most crucial attributes of a chemical sensor is its selectivity, which refers to the sensor's ability to differentiate between two chemical species with similar molecular properties.[1] Traditional molecular recognition methods, based on room temperature reversible adsorption on immobilized chemical interfaces (receptors) on sensor surfaces, often suffer from poor selectivity due to the generic nature of weak chemical interactions.[2,3] Additionally, nonuniformity in immobilized functional coatings can lead to unacceptable sensor-to-sensor response variability.[4−6] The latter is even more pronounced in micro- and nanosensors compared to macrosensors, such as quartz crystal microbalances (QCM), due to their smaller surface areas.[6,7] The limited selectivity of miniature sensors remains a significant obstacle to their wider adoption and commercialization. As a result, enhancing the sensitivity and selectivity of these sensors has become a primary focus in the field,[8−12] encompassing both classical and emerging quantum sensors.[13−16]

In an effort to overcome the issue of insufficient chemical selectivity, studies have focused on the combination of microfabricated structures, including microcantilevers and microstrings, with infrared (IR) spectroscopy.[17−19] This approach aims to enhance chemical sensors' selectivity and sensitivity by leveraging the microfabricated structures' unique properties and advantages of IR spectroscopy. Detailed information about adsorbed materials' chemical composition and molecular structure can be obtained in the mid-IR region (~4000−4000 cm^{-1}) encompassing the characteristic absorption bands of various functional groups and bonds present in organic and inorganic compounds.[20] The NIR region (~4000−12500 cm^{-1}), while having its own advantages in certain cases, is dominated by overtones and combination bands of the fundamental vibrations, which can lead to broad, overlapping bands, making the interpretation of spectral features more challenging.[21−23]

Microstructures, known for their sensitive transduction of temperature variations, provide an excellent platform for photothermal and photoacoustic spectroscopy.[24,25] Layered structures with differing thermal properties can undergo deformation, when interacting both directly with IR radiation and indirectly through the nonradiative decay of adsorbed molecules excited by IR radiation. For instance, bimaterial cantilevers and microstrings have been reported to generate the spectrum of the radiation source, as well as the spectra of adsorbed molecules interacting with the excitation radiation, due to the development of asymmetric stress distribution.[26,27] The observed signals effectively display both the mechanical resonance spectrum of the oscillator (e.g., when the source is properly amplitude modulated) and the molecular resonance spectrum when the source is tuned spectrally. One advantage of these techniques is their receptor-free operation. However, the sensitivity relies on the thermal capacitance of the sensor,

Received: May 8, 2023
Revised: August 9, 2023

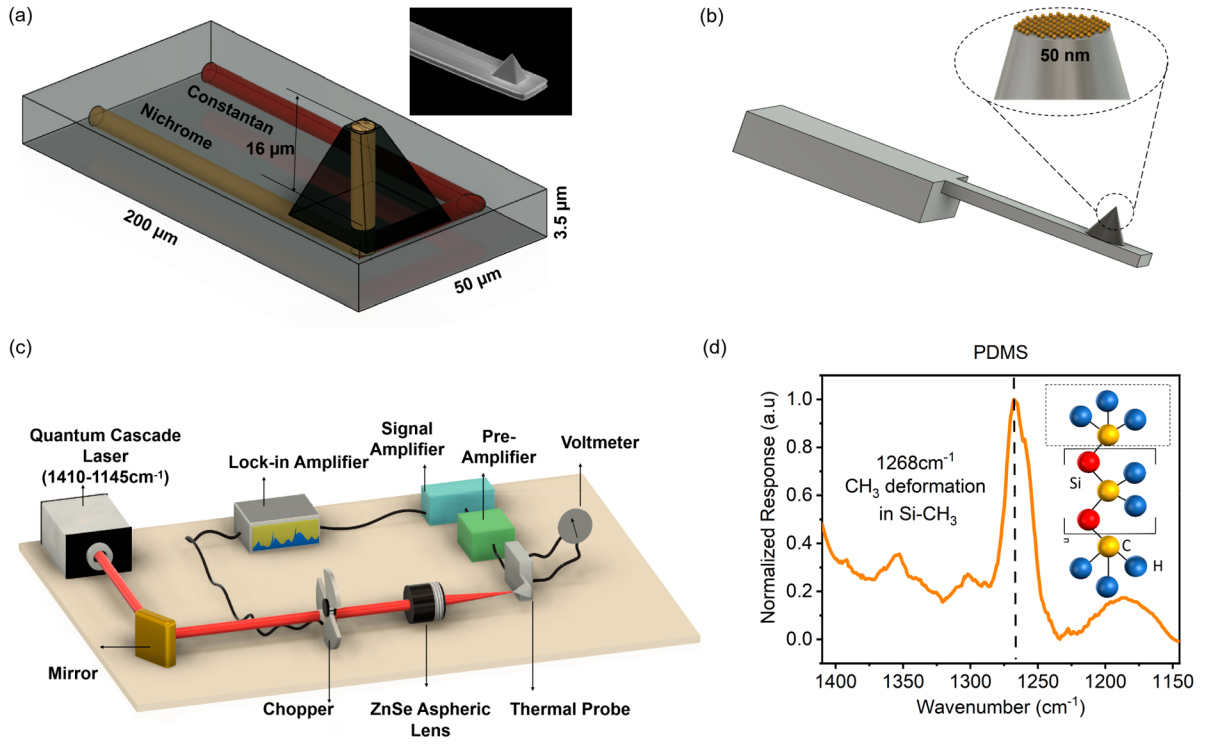

Figure 1. Tip-adsorbed photothermal spectroscopy (TAPS). (a) Schematics of the embedded thermocouple on the tip of the thermal probe (image acquired with a focused ion beam during fabrication). (b) Illustration of the molecular adsorption on a 50 nm diameter tip. (c) Schematics of the experimental setup. (d) TAPS measurement of the PDMS.

meaning that higher (heat) energies are needed to increase the sensor temperature. Consequently, the technique's sensitivity is limited by the mass of the device.[18,19]

The prevalent use of microcantilever probes in various scanning probe microscopy (SPM) applications and the growing interest in localized temperature measurements have spurred the development of cantilevers with nanoscale thermocouples integrated into their tip regions.[28,29] For instance, in scanning thermal microscopy (SThM), these specialized probes are utilized for the thermal mapping of samples.[30−32] The embedded thermocouples possess low thermal capacitance, meaning that they do not exhibit high heat absorption and storage. SThM cantilevers, commonly used for surface temperature measurement and thermomechanical actuation, exhibit a high room-temperature resolution of approximately 40 mK.[28] While this sensitivity is somewhat inferior to that of an optimized bimaterial cantilever (~10 mK), its active sensor area can be roughly 10^{12} times smaller.[28] Because the thermocouple is located at the free end of the thermal probe, it benefits from better insulation from the cantilever's massive (heatsink) base, providing higher thermal resistance.

In this Letter, we aim to showcase a sensitive spectroscopic technique based on the thermoelectric measurement of physisorbed molecules on a nanothermocouple embedded within a thermal probe. The thermoelectric effect consists of two primary phenomena: the Seebeck effect and the Peltier effect. The Seebeck effect refers to the generation of a voltage difference in a material due to the presence of a temperature gradient, while the Peltier effect is the reverse process, where a voltage applied across a material creates a temperature difference. We leverage the fact that the temperature difference between the hot and cold leads plays a crucial role in driving the thermoelectric effect, while the temperature profile along the lengths of the materials can be optimized for improved performance.

In our probe, two distinct metals are deposited as individual stripes on a silicon cantilever and meet near the free end of the cantilever to form a nanojunction (thermocouple). The other ends of the spatially separated metal stripes form contact electrodes on the cantilever chip's base (Figure 1). Assuming the base remains at room temperature due to its large thermal capacitance, the thermocouple junction forms an "active window" near the tip. When the junction's temperature increases above room temperature, a voltage can be detected between the room-temperature metal electrodes on the cantilever's base.

Upon exposure to IR radiation, the nanoscale junction locally probes the heat generated by the nonradiative decay of physisorbed molecules on the tip, leading to a measurable electric potential difference. Qualitatively, we can describe the process by denoting the photothermally generated heat by ΔQ, assuming that it is contributed solely by the molecules at or near the tip thermocouple. Consequently, ΔQ is released into a tip volume Ω_{tc} containing the embedded thermocouple. We expect the temperature change ΔT in Ω_{tc} to be $\Delta Q/mC$, where m is the mass of Ω_{tc} and C is its heat capacity. In response to ΔT, a voltage difference ΔV is induced between the reference contact electrodes at the cantilever's base, which is then amplified for readout and display. A well-insulated device with a small thermal mass can produce a large ΔT for a small ΔQ. Because $\Delta Q = \Delta Q(\lambda,P)$, where λ is the illumination wavelength and P is the incident IR radiation power absorbed by the molecules, the absorption spectrum of the tip adsorbates may be obtained from the thermal probe readout. We will now proceed to experimentally demonstrate the

https://doi.org/10.1021/acs.nanolett.3c01710
Nano Lett. XXXX, XXX, XXX−XXX

described "tip-adsorbed" photothermal spectroscopy (TAPS) and theoretically analyze the underlying mechanism. Specifically, we computationally obtained reasonable agreement with the experiments and suggested how to optimize the design.

As shown in Figure 1a, TAPS is implemented using a Si cantilever (length 200 μm, width 50 μm, and thickness 3.5 μm) with a 25 nm radius thermocouple embedded in its pyramidal tip. The metal leads of the thermocouple, deposited on the cantilever, are thermally insulated by a thin SiO_2 layer, as explained in the Experimental Details section. Two different methods were used to deposit the target material onto the probe: (A) via AFM imaging, wherein islands of deposited TNT on a surface are contacted by the probe; and (B) by directly populating the tip with TNT and DMMP via physical vapor deposition (PVD). Details of the sample deposition are given in Section S1.2. Using the PVD, we also investigated polymers polydimethylsiloxane (PDMS) and poly(methyl methacrylate) (PMMA) owing to their unique IR absorption peaks in the spectral window considered.

The excited molecular states decay by emitting photons (radiative process) or, in the present case, predominantly by producing heat (nonradiative decay). A quantum cascade laser (QCL), tunable at $1145 \leq \upsilon\ [cm^{-1}] \leq 1410$, was used as the source. A calibration was performed by measuring the TAPS signal caused by a known temperature, yielding 45 mV/K. Because the output power of the employed QCL is not constant across its spectral window (shown in the Supporting Information), our background spectral correction receives contributions from the signal with no adsorbate as well as from the wavelength-dependent power profile of the source. To further validate the TAPS spectroscopic signal transduction, we performed Fourier transform IR spectroscopy (FTIR) in the attenuated total reflection (ATR) configuration.

The results are listed in Figures 1−4. The QCL output beam was amplitude modulated at 50 Hz to allow lock-in detection of the probe response (see schematics in Figure 1c). Figure 1d shows the TAPS response when the sensor has been exposed to TNT. The TNT spectra were further explored with TAPS in Figure 2a via method A: AFM method, and in Figure 2b via method B: PVD method, for comparison and in Figure 2c using the standard FTIR for validation. The observed photothermal band with a peak at 1376 cm^{-1} in Figure 2 exhibits the characteristics of the NO_2 stretching vibration of the TNT.

Photothermal signal represents the combined effect of adsorbed mass, de-excitation pathways of the molecules, and IR intensity. Therefore, our mass estimates are species-specific and not absolute. The added mass was insufficient for the mechanical resonance frequency of the cantilever (first frequency of 135 kHz with an estimated sensitivity of 1.2 ng/kHz; see the Supporting Information) to exhibit a shift. Assuming a 1.2 ng/kHz sensitivity, a significantly higher mass than that observed in the thermoelectric measurements would be needed to detect a shift. The TAPS spectra generated using an IR laser may feature peaks that are not apparent in the FTIR spectra. Such differences are likely in part due to the different background correction procedures. In the FTIR bulk-level measurements, each acquired spectrum is corrected with that of the background (i.e., atmosphere and substrate without the specimen). In the proof-of-principle TAPS microscale measurements, to correct each spectrum, the probe must be removed, coated, and replaced. Additionally, in the TAPS setup, the QCL generates a linearly polarized beam in a single

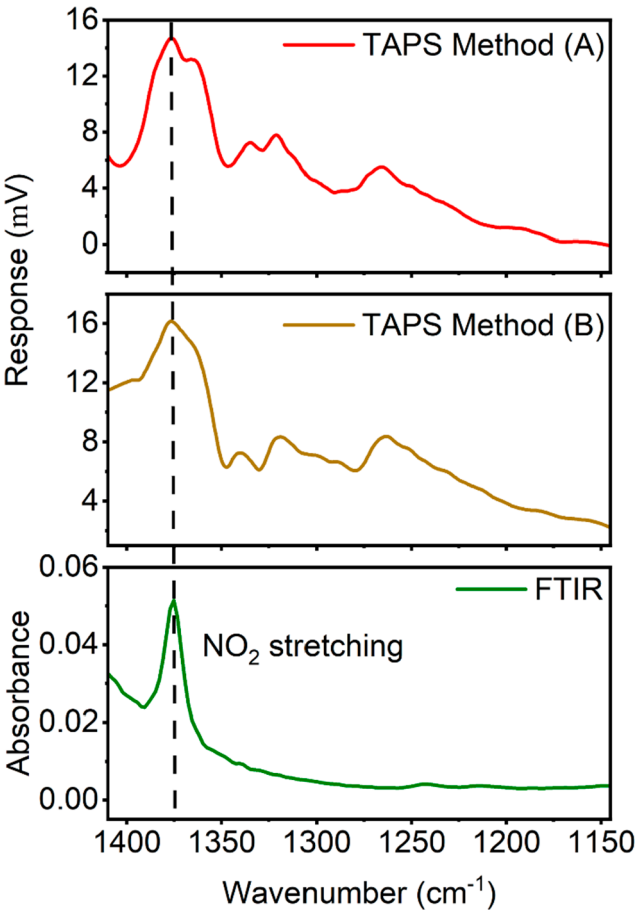

Figure 2. Comparison between TAPS and FTIR spectra of TNT. TAPS spectra exhibit additional features not observed in the FTIR spectrum. The TAPS spectra shown correspond to the two deposition methods A and B, that is, AFM image and PVD, respectively. The experimental setup amplifies the TAPS signal from μV to mV. (c) FTIR spectrum of TNT obtained under attenuated total reflection (ATR) condition. The single vibrational peak observed corresponds to the stretching of NO_2.

spatial mode, nominally TEM_{00} with a line width ≤100 MHz at FWHM when measured over 1 s with a wavelength accuracy ≤1 cm^{-1}. The FTIR system employed (Bruker VERTEX 70, Billerica, MA), on the other hand, achieves sample excitation using a thermal source in an interferometric configuration that generates an unpolarized beam with a spectral resolution, here selected to be 4 cm^{-1}. Furthermore, in FTIR spectroscopy, one determines the absorption of IR light by a sample (Beer−Lambert) by measuring the remaining transmitted or unabsorbed photons using photodetectors. In the TAPS technique, on the other hand, one detects IR light by the cantilever responding to the heat generated through photon absorption. As such, TAPS represents a direct and complementary calorimetric technique, in contrast to the conventional detection of photons not absorbed by the sample.

Figure 3a shows the TAPS spectrum of DMMP and its comparison with the FTIR spectrum (averaged 100 times per scan). The TAPS spectrum of PMMA is shown in Figure 3b, while Figure 3c shows the spectrum of PDMS. An excellent agreement is observed between the TAPS and FTIR results, demonstrating the high spectral selectivity of TAPS. The observed photothermal band with a peak at 1376 cm^{-1} in Figure 3a exhibits the characteristics of the P═O stretching

https://doi.org/10.1021/acs.nanolett.3c01710
Nano Lett. XXXX, XXX, XXX−XXX

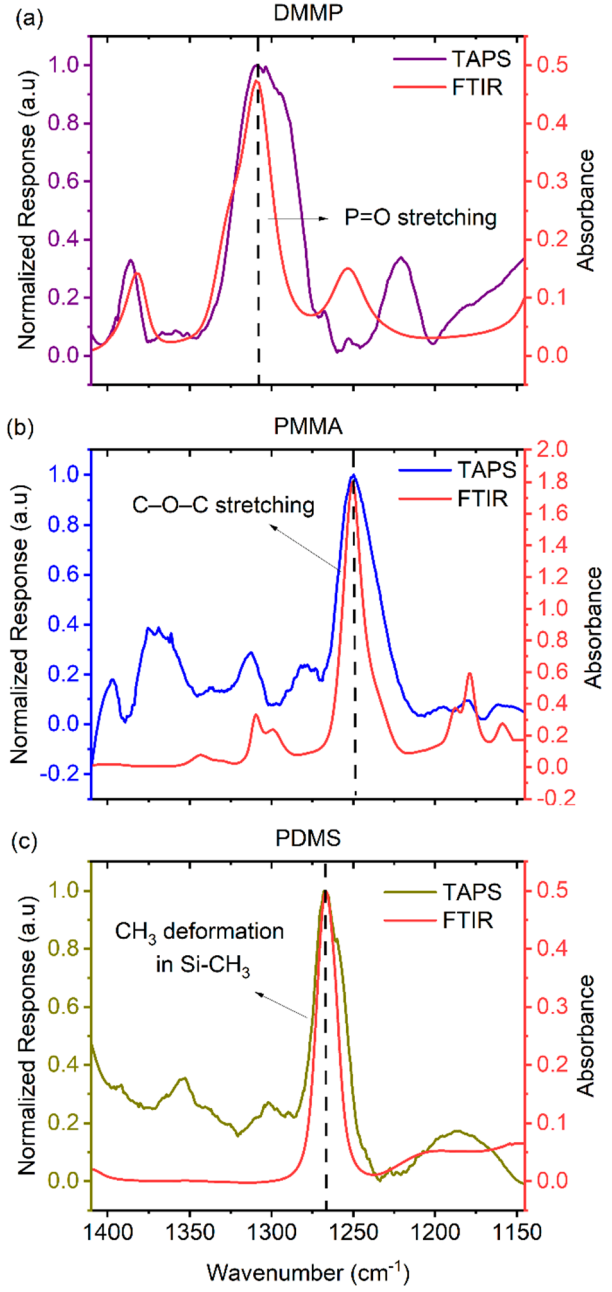

Figure 3. TAPS versus FTIR spectroscopy: (a) DMMP, (b) PMMA, and (c) PDMS. All analytes were deposited via physical vapor deposition.

mode of DMMP, while the peak at 1264 cm^{-1} in Figure 3b belongs to the C−O−C stretching of PMMA. The peak at 1268 cm^{-1} in Figure 3c is assigned to CH_3 deformation in Si−CH_3 of PDMS. The line widths of the TAPS spectra appear broader than those observed in the FTIR measurements. In general, the broadening of the peaks in conventional solid and liquid phase IR spectra, such as seen in the FTIR spectra here, is caused by the relaxation and dephasing of the excited vibrational states and indicates the complex, fast dynamic interaction of the molecule with its environment. Broadening effects can reduce spectral differentiation. With optimization and machine learning,[33] spectral differentiation could be improved. Clearly, in the case of TAPS spectra, other broadening mechanisms are at play, warranting further exploration.

We also note that when using the PVD-prepared cantilevers, the adsorbates located away from the tip may affect the junction temperature, given the QCL beam diameter of 2.5 mm. To support the argument that the Seebeck signal originates mainly from the thermocouple region of the cantilever, we displaced the laser beam to alter the excitation region. No thermoelectric signal could be observed when the thermocouple surface was excluded. The lack of a potential difference when exposing the cantilever surface but not the thermocouple demonstrates that the spectroscopic signal originates mainly from the tip. The cantilever's SiO_2 layer provides a barrier to the transfer of heat to the thermocouple leads. Because the (cold) reference point for the thermocouple is limited to the comparatively massive base of the cantilever, it remains at ambient temperature (here, room temperature of 293 K). The mass of the cantilever is ∼19 ng while the base of the cantilever is ∼75 μg. The experiments demonstrate that the tip is the main sensitive area, and the base of the cantilever has a negligible contribution to the Seebeck voltage. These arguments are corroborated by our analysis of the computationally obtained solutions, as detailed in the model below.

To develop a model for the observed effect, we investigated the factors that could contribute to the TAPS signal. Importantly, how the photothermally generated temperature varies with the quantity of adsorbed material must be determined. The thermocouple temperature can be measured with a sensitivity of 0.01 °C using a low-noise electronic module (VertiSense, AppNano, Mountain View, CA), typically used as a thermal imaging amplifier in SThM. A simple noise analysis gives $N_{thermal} \sim 130-900$ nV, which is sufficiently smaller than the TAPS signal (Supporting Information). The result, displayed in Figure 4a, verifies the expected dependence of temperature increases with the increase in the quantity of the adsorbates. A positive correlation was also found between the TAPS signal and the laser power, as shown in Figure 4b. We note here that the use of the QCM-based gravimetric measurement, yielding a relatively low sensitivity, provides an estimate of the "adsorption rate" rather than an absolute mass calibration.

To further elucidate both the thermal and thermoelectric responses of the TAPS sensor and to illustrate how the system can be tailored for optimal performance, we conducted a computational analysis. By modeling the entire sensor system, the system's behavior can be investigated under parametric conditions. The tip is made of SiO_2 and incorporates two metal substructures made of constantan and nichrome that form the two thermoelectric junctions. Obtaining the stationary thermal response of the cantilever part (sans the tip) is trivial and is not treated here, as it is not critical to the thermoelectric events. Assume the sensor consists of N layers occupying the spatial domains Ω_i, $i = 1-N$. Prior to experiments, the sensor is at room temperature, an ambient pressure of 1 Pa, and zero relative humidity so that the initial condition may be taken to be $T(\mathbf{x},t)|_{t=0} = T_0 = 293.15$ K, for each sensor point $\forall \mathbf{x} \in \Omega_i$, prior to the arrival of the first QCL pulse. All boundaries (normal vector $\mathbf{n}$), except for the tip boundary, are assumed to have zero heat flux $\boldsymbol{\phi}$; that is, they are thermally insulated ($\mathbf{n}\cdot\boldsymbol{\phi} = 0$). We assume no other sources of radiation interacts with the adsorbates. Note that the domains Ω_i here account for all of the fabrication material layers occupied by sensor domain Ω. Given that any temperature rises above T_0, caused by the QCL

https://doi.org/10.1021/acs.nanolett.3c01710
Nano Lett. XXXX, XXX, XXX−XXX

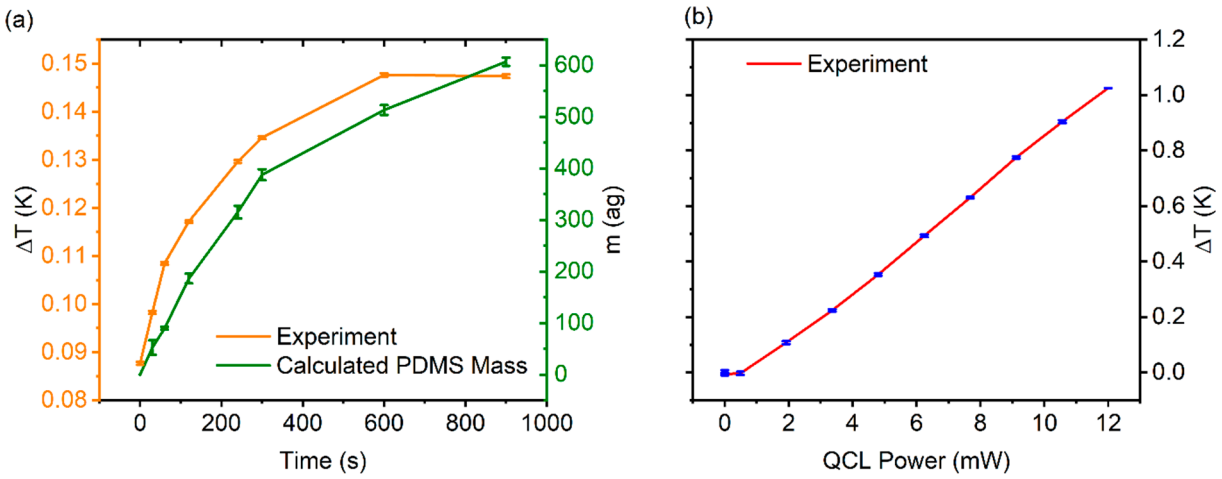

Figure 4. (a) Photothermally induced temperature changes in TAPS as a function of time and calculated adsorbed PDMS mass on the tip of the probe as a function of time. The adsorbed mass is estimated from the adsorption rate determined using a QCM in an identical setup. (b) Temperature changes in TAPS as a function of QCL output power. The experiments were conducted with a thermocouple with 384 ag of PDMS. Error bars are shown in blue.

pulses, follows $T(t)/T_0 = 1 + \delta(t)$, where δ is small and depends on the amplitude modulation of the QCL beam, we assume any radiative heat transfer to be negligible. Additionally, because the probe's surface area is also small, we neglect any heat transfer by convection. Preliminary computational results can readily show that the heat transport through Ω occurs on time scales faster than ms. For the undriven cantilever subject only to noise, dissipative effects, other than the Joule heating, such as thermoelasticity do not contribute to the temperature distribution. Therefore, for the QCL amplitude modulation frequencies considered in this work, $f_{QCL} \sim 50$ Hz, we need to solve only the stationary $(\partial_t T \to 0)$ heat equation sourced by the field-induced and temperature-induced (Seebeck) currents $\mathbf{J}$ and no Peltier term:

$$\nabla\cdot[k(\mathbf{x}, T)\nabla T(\mathbf{x})] = -\mathbf{J}\cdot\mathbf{E} = -[-\sigma(\mathbf{x}, T)\nabla V(\mathbf{x}) - \sigma(\mathbf{x}, T)S(\mathbf{x}, T)\nabla T(\mathbf{x})]\cdot[-\nabla V(\mathbf{x})] \quad (1)$$

where V is the electric scalar potential of the field $\mathbf{E}$, and σ and k are the electric and thermal conductivities, respectively, while S denotes the Seebeck coefficient of a domain. Here, $V = 0$ is understood as the initial value of the potential, corresponding to the temperature uniformity. With no other charges present, we note the current is conserved; thus

$$\nabla\cdot\mathbf{J} = \nabla\cdot[-\sigma_\Omega(T)\nabla V - \sigma_\Omega S_\Omega \nabla T(\mathbf{x})] = 0 \quad (2)$$

where at the sensor outer boundaries, we assume no transport ($\mathbf{n}\cdot\mathbf{J} = 0$). We assume $V = 0$ V for the potential on the end boundary (terminal) of the constantan layer, while the start boundary (tip radius $R = 25$ nm) may be modeled as an unconnected perfect conductor. While heat loss due to conduction through the wire and silicon dioxide layer is fully accounted for, we note that here the radiative heat loss (considering the nanosized sensor at $T \approx T_0$) is generally much smaller than losses due to conduction or convection. A simple estimation using cantilever parameters shows that conduction through the base and the chip is the dominant mode of heat transfer for TAPS (see the Supporting Information)

If the IR radiation is instantly absorbed by the absorbates, which leads to $\delta = 3.4 \times 10^{-3}$, or a tip temperature just one degree above the initial temperature, a reasonable assumption based on the experimental observations, we obtain the temperature and thermoelectric potential distributions by solving the thermoelectric equations (see the Supporting Information for details). We will first consider an overall metal electrode arrangement likely to be implemented in sensors such as that experimented with here. The results are shown in Figure 5. For a pyramidal tip, a good estimate of the thermal response is computed in Figure 5. These results require 3D meshing of the model tip. Because for a conical tip only negligible deviation is expected when compared to a pyramidal tip, we also compute the conical case in which the cylindrical symmetry can be utilized to reduce the computational burden. The results are shown in Figure 5. These results are consistent with the experimental observations and demonstrate how the design of more specialized sensors can be achieved.

In conclusion, the presented photothermal generation of spectral data by TAPS is found to facilitate robust metrology for small adsorbate quantities. The results suggest that the observed attogram detection limit for molecular recognition of physisorbed molecules can be improved with additional nanofabrication optimization and design innovation, including the exploration of new materials for thermal management in the neighborhood of the tip region. Given that the QCL technology could offer line widths as narrow as 0.00002 cm^{-1} or ~0.5 MHz,[34] spectral optimization can be further explored. The employed thermal probe, fabricated to incorporate a nanothermocouple, can therefore be viewed as a sensor platform for the detection of an exceedingly small number of adsorbates. Concluding that only the molecules adsorbed on the thermocouple tip surface of the thermal probe produce the observed IR spectral response is a major finding and impetus in favor of such a platform. In addition, because excitation/deexcitation times are orders of magnitude smaller than the time of temperature measurements, an extremely small number of molecules could be detected by increasing the fluence of the excitation source. Therefore, by optimizing the thermal mass, thermal conductance, irradiation time, and IR fluence, this method can provide exciting opportunities for developing high-performance sensors with very high sensitivity, selectivity, and ease of operation. The presented computational results demonstrate that design based on incorporating such material

https://doi.org/10.1021/acs.nanolett.3c01710
Nano Lett. XXXX, XXX, XXX−XXX

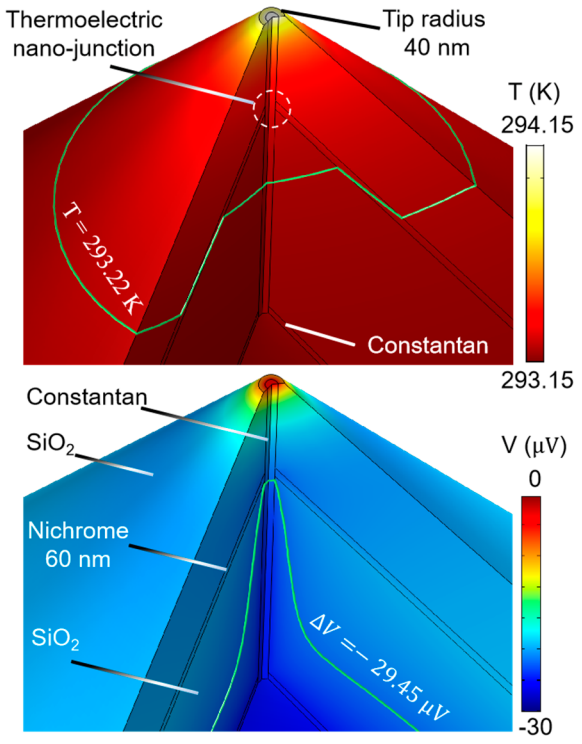

Figure 5. Computational study of the thermoelectric properties of TAPS. The temperature (top) is visualized by opening a section of the tip to display the interior distribution. The lower part of the tip and the cantilever are excluded for visual clarity. A single contour level at 293.22 K is provided to better elucidate the significant temperature discontinuity caused by the various layers. The dashed circle indicates the location of the thermoelectric junction. Owing to the nonzero Seebeck coefficients of the annotated materials, the computed temperature distribution induces an electric potential distribution (bottom). The single contour at −29.45 μV illustrates the behavior of the potential formed near the junction. Experimental setup amplifies the signal to mV.

and geometry optimization strategies is possible via parametric studies of a 3D model that accurately accounts for all nanoscale material layers and shapes. For example, we envision the fabrication of multiple junctions within an advanced tip or one in which a Peltier subsystem could also be integrated with the Seebeck subsystem to allow for the creation of a higher temperature gradient.

■ ASSOCIATED CONTENT

Supporting Information

The Supporting Information is available free of charge at https://pubs.acs.org/doi/10.1021/acs.nanolett.3c01710.

Additional details on the nanothermal probe, TAPS experimental arrangement, photothermal spectroscopy, the comparison of performance between the bimaterial cantilever and nanothermal probe, a detailed analysis of experimental data on another set of nanoprobes, QCL power profile, calculations of adsorbed mass on the nanoprobe, and the computational model (PDF)

■ AUTHOR INFORMATION

Corresponding Author

Thomas Thundat − *Chemical and Biological Engineering, University at Buffalo, Buffalo, New York 14260, United States;* orcid.org/0000-0003-1721-1181; Email: tgthunda@buffalo.edu

Authors

Yaoli Zhao − *Chemical and Biological Engineering, University at Buffalo, Buffalo, New York 14260, United States*

Patatri Chakraborty − *Chemical and Biological Engineering, University at Buffalo, Buffalo, New York 14260, United States*

Ali Passian − *Quantum Computing and Sensing Group, Computational Sciences and Engineering Division, Oak Ridge National Laboratory, Oak Ridge, Tennessee 37831, United States;* orcid.org/0000-0002-4736-4157

Complete contact information is available at: https://pubs.acs.org/10.1021/acs.nanolett.3c01710

Notes

The authors declare no competing financial interest.

■ ACKNOWLEDGMENTS

This work was supported by the School of Engineering and Applied Sciences (SEAS) University at Buffalo, The State University of New York, and NSF Award 2226614. A.P. acknowledges partial support from the Office of Biological and Environmental Research (BER) in the U.S. Department of Energy (DOE) Office of Science. ORNL is managed by UT-Battelle, LLC, for the US DOE under Contract DE-AC05-00OR22725. The authors acknowledge Drs. A. Ciric and M. Medic, the Institute of Nuclear Sciences, the University of Belgrade, for help with the physical vapor deposition setup and Dr. A. Chand from AppNano for fruitful discussions.

■ REFERENCES

(1) Murray, R. W. Chemical Sensors and Molecular Selectivity. *Anal. Chem.* **1994**, *66* (9), A505−A505.

(2) Strle, D.; Stefane, B.; Trifkovic, M.; Van Miden, M.; Kvasic, I.; Zupanic, E.; Musevic, I. Chemical Selectivity and Sensitivity of a 16-Channel Electronic Nose for Trace Vapour Detection. *Sensors-Basel* **2017**, *17* (12), 2845.

(3) Hsieh, M. D.; Zellers, E. T. Limits of recognition for simple vapor mixtures determined with a microsensor array. *Anal. Chem.* **2004**, *76* (7), 1885−1895.

(4) Desikan, R.; Armel, S.; Meyer, H. M.; Thundat, T. Effect of chain length on nanomechanics of alkanethiol self-assembly. *Nanotechnology* **2007**, *18* (42), 424028.

(5) Godin, M.; Williams, P. J.; Tabard-Cossa, V.; Laroche, O.; Beaulieu, L. Y.; Lennox, R. B.; Grutter, P. Surface stress, kinetics, and structure of alkanethiol self-assembled monolayers. *Langmuir* **2004**, *20* (17), 7090−7096.

(6) Patil, S. B.; Al-Jehani, R. M.; Etayash, H.; Turbe, V.; Jiang, K.; Bailey, J.; Al-Akkad, W.; Soudy, R.; Kaur, K.; McKendry, R. A.; Thundat, T.; Ndieyira, J. W. Modified cantilever arrays improve sensitivity and reproducibility of nanomechanical sensing in living cells. *Commun. Biol.* **2018**, *1* (1), 175.

(7) Sartore, L.; Barbaglio, M.; Borgese, L.; Bontempi, E. Polymer-grafted QCM chemical sensor and application to heavy metal ions real time detection. *Sensor Actuat B-Chem.* **2011**, *155* (2), 538−544.

(8) Cao, Z. X.; Yao, B. C.; Qin, C. Y.; Yang, R.; Guo, Y. H.; Zhang, Y. F.; Wu, Y.; Bi, L.; Chen, Y. F.; Xie, Z. D.; et al. Biochemical sensing in graphene-enhanced microfiber resonators with individual molecule sensitivity and selectivity. *Light-Sci. Appl.* **2019**, *8*, 107.

(9) Kummer, A. M.; Hierlemann, A.; Baltes, H. Tuning sensitivity and selectivity of complementary metal oxide semiconductor-based capacitive chemical microsensors. *Anal. Chem.* **2004**, *76* (9), 2470−2477.

(10) Qi, P.; Vermesh, O.; Grecu, M.; Javey, A.; Wang, Q.; Dai, H.; Peng, S.; Cho, K. J. Toward large arrays of multiplex functionalized carbon nanotube sensors for highly sensitive and selective molecular detection. *Nano Lett.* **2003**, *3* (3), 347−351.
(11) Azizi, A.; Dogan, M.; Long, H.; Cain, J. D.; Lee, K.; Eskandari, R.; Varieschi, A.; Glazer, E. C.; Cohen, M. L.; Zettl, A. High-Performance Atomically-Thin Room-Temperature NO2 Sensor. *Nano Lett.* **2020**, *20* (8), 6120−6127.
(12) Hwang, Y.; Sohn, H.; Phan, A.; Yaghi, O. M.; Candler, R. N. Dielectrophoresis-Assembled Zeolitic Imidazolate Framework Nanoparticle-Coupled Resonators for Highly Sensitive and Selective Gas Detection. *Nano Lett.* **2013**, *13* (11), 5271−5276.
(13) Foy, C.; Zhang, L. N.; Trusheim, M. E.; Bagnall, K. R.; Walsh, M.; Wang, E. N.; Englund, D. R. Wide-Field Magnetic Field and Temperature Imaging Using Nanoscale Quantum Sensors. *Acs Appl. Mater. Inter* **2020**, *12* (23), 26525−26533.
(14) Andrich, P.; Li, J. J.; Liu, X. Y.; Heremans, F. J.; Nealey, P. F.; Awschalom, D. D. Microscale-Resolution Thermal Mapping Using a Flexible Platform of Patterned Quantum Sensors. *Nano Lett.* **2018**, *18* (8), 4684−4690.
(15) Gao, X.; Jiang, B.; Llacsahuanga Allcca, A. E.; Shen, K.; Sadi, M. A.; Solanki, A. B.; Ju, P.; Xu, Z.; Upadhyaya, P.; Chen, Y. P.; Bhave, S. A.; Li, T. High-Contrast Plasmonic-Enhanced Shallow Spin Defects in Hexagonal Boron Nitride for Quantum Sensing. *Nano Lett.* **2021**, *21* (18), 7708−7714.
(16) Kongsuwan, N.; Xiong, X.; Bai, P.; You, J. B.; Png, C. E.; Wu, L.; Hess, O. Quantum Plasmonic Immunoassay Sensing. *Nano Lett.* **2019**, *19* (9), 5853−5861.
(17) Chae, I.; Lee, D.; Kim, S.; Thundat, T. Electronic Nose for Recognition of Volatile Vapor Mixtures Using a Nanopore-Enhanced Opto-Calorimetric Spectroscopy. *Anal. Chem.* **2015**, *87* (14), 7125−7132.
(18) Krause, A. R.; Van Neste, C.; Senesac, L.; Thundat, T.; Finot, E. Trace explosive detection using photothermal deflection spectroscopy. *J. Appl. Phys.* **2008**, DOI: 10.1063/1.2908181.
(19) Biswas, T. S.; Miriyala, N.; Doolin, C.; Liu, X.; Thundat, T.; Davis, J. P. Femtogram-Scale Photothermal Spectroscopy of Explosive Molecules on Nanostrings. *Anal. Chem.* **2014**, *86* (22), 11368−11372.
(20) Prashanthi, K.; Phani, A.; Thundat, T. Photothermal Electrical Resonance Spectroscopy of Physisorbed Molecules on a Nanowire Resonator. *Nano Lett.* **2015**, *15* (8), 5658−5663.
(21) Itkis, M. E.; Perea, D. E.; Niyogi, S.; Rickard, S. M.; Hamon, M. A.; Hu, H.; Zhao, B.; Haddon, R. C. Purity evaluation of as-prepared single-walled carbon nanotube soot by use of solution-phase near-IR spectroscopy. *Nano Lett.* **2003**, *3* (3), 309−314.
(22) Shih, W. C.; Santos, G. M.; Zhao, F.; Zenasni, O.; Arnob, M. M. Simultaneous Chemical and Refractive Index Sensing in the 1−2.5 mum Near-Infrared Wavelength Range on Nanoporous Gold Disks. *Nano Lett.* **2016**, *16* (7), 4641−4647.
(23) Welsher, K.; Liu, Z.; Daranciang, D.; Dai, H. Selective probing and imaging of cells with single walled carbon nanotubes as near-infrared fluorescent molecules. *Nano Lett.* **2008**, *8* (2), 586−590.
(24) Barnes, J. R.; Stephenson, R. J.; Welland, M. E.; Gerber, C.; Gimzewski, J. K. Photothermal Spectroscopy with Femtojoule Sensitivity Using a Micromechanical Device. *Nature* **1994**, *372* (6501), 79−81.
(25) Kim, S.; Lee, D.; Thundat, T. Photothermal cantilever deflection spectroscopy. *EPJ Tech Instrum* **2014**, *1* (1), 7.
(26) Bagheri, M.; Chae, I.; Lee, D.; Kim, S.; Thundat, T. Selective detection of physisorbed hydrocarbons using photothermal cantilever deflection spectroscopy. *Sens. Actuators, B* **2014**, *191*, 765−769.
(27) Yamada, S.; Schmid, S.; Larsen, T.; Hansen, O.; Boisen, A. Photothermal Infrared Spectroscopy of Airborne Samples with Mechanical String Resonators. *Anal. Chem.* **2013**, *85* (21), 10531−10535.
(28) Shekhawat, G. S.; Ramachandran, S.; Sharahi, H. J.; Sarkar, S.; Hujsak, K.; Li, Y.; Hagglund, K.; Kim, S.; Aden, G.; Chand, A.; et al. Micromachined Chip Scale Thermal Sensor for Thermal Imaging. *ACS Nano* **2018**, *12* (2), 1760−1767.
(29) Goeckeritz, J.; Aden, G. D.; Chand, A.; Willard, J. F. Vertical embedded sensor and process of manufacturing thereof. USA US9389244B2, 2016.
(30) Mills, G.; Zhou, H.; Midha, A.; Donaldson, L.; Weaver, J. M. R. Scanning thermal microscopy using batch fabricated thermocouple probes. *Appl. Phys. Lett.* **1998**, *72* (22), 2900−2902.
(31) Shi, L.; Plyasunov, S.; Bachtold, A.; McEuen, P. L.; Majumdar, A. Scanning thermal microscopy of carbon nanotubes using batch-fabricated probes. *Appl. Phys. Lett.* **2000**, *77* (26), 4295−4297.
(32) Kim, K.; Chung, J.; Hwang, G.; Kwon, O.; Lee, J. S. Quantitative Measurement with Scanning Thermal Microscope by Preventing the Distortion Due to the Heat Transfer through the Air. *ACS Nano* **2011**, *5* (11), 8700−8709.
(33) Zhu, J. X.; Ren, Z. H.; Lee, C. Toward Healthcare Diagnoses by Machine-Learning-Enabled Volatile Organic Compound Identification. *ACS Nano* **2021**, *15* (1), 894−903.
(34) Ganser, H.; Frech, B.; Jentsch, A.; Mürtz, M.; Gmachl, C.; Capasso, F.; Sivco, D. L.; Baillargeon, J. N.; Hutchinson, A. L.; Cho, A. Y.; et al. Investigation of the spectral width of quantum cascade laser emission near 5.2 μm by a heterodyne experiment. *Opt. Commun.* **2001**, *197* (1), 127−130.

https://doi.org/10.1021/acs.nanolett.3c01710
Nano Lett. XXXX, XXX, XXX−XXX